UCSF

UC San Francisco Previously Published Works

Title

Super-resolution microscopy reveals that disruption of ciliary transition-zone architecture causes Joubert syndrome

Permalink

Journal

ISSN

Authors

Shi, Xiaoyu
Garcia, Galo
Van De Weghe, Julie C
et al.

Publication Date

DOI

Peer reviewed

Super-resolution microscopy reveals that disruption of ciliary transition zone architecture is a cause of Joubert syndrome

Xiaoyu Shi[1,2], **Galo Garcia III**[1,3,4], **Julie C. Van De Weghe**[5], **Ryan McGorty**[2,7], **Gregory J. Pazour**[6], **Dan Doherty**[5], **Bo Huang**[2,3,8,*], and **Jeremy F. Reiter**[3,4,*]

[2]Department of Pharmaceutical Chemistry, University of California, San Francisco, San Francisco, CA 94143, USA

[3]Department of Biochemistry and Biophysics, University of California, San Francisco, San Francisco, CA 94143, USA

[4]Cardiovascular Research Institute, University of California, San Francisco, San Francisco, CA 94143, USA

[5]Department of Pediatrics, University of Washington Medical Center, Seattle, WA 98195, USA

[6]Program in Molecular Medicine, University of Massachusetts Medical School, Biotech II, Suite 213, 373 Plantation Street, Worcester, MA, USA

[8]Chan Zuckerberg Biohub, San Francisco, CA 94158 USA

Abstract

Ciliopathies, including nephronophthisis (NPHP), Meckel syndrome (MKS) and Joubert syndrome (JBTS), can be caused by mutations affecting components of the transition zone, a ciliary domain near its base that controls the protein composition of its membrane. We defined the three-dimensional arrangement of key proteins in the transition zone using two-color stochastic optical reconstruction microscopy (STORM). NPHP and MKS complex components form nested rings comprised of nine-fold doublets. JBTS-associated mutations in *RPGRIP1L* or *TCTN2* displace select transition zone proteins. Diverse ciliary proteins accumulate at the transition zone in wild type cells, suggesting that the transition zone is a waypoint for proteins entering and exiting the cilium. JBTS-associated mutations in *RPGRIP1L* disrupt SMO accumulation at the transition zone and the ciliary localization of SMO. We propose that the disruption of transition zone architecture in JBTS leads to a failure of SMO to accumulate at the transition zone, disrupting developmental signaling in JBTS.

INTRODUCTION

Cilia are cellular projections generated from a basal body, a cylinder comprised of triplet microtubules arranged with nine-fold symmetry[1–4]. The microtubules that project distally from the basal body form the ciliary axoneme[5]. The axoneme is ensheathed by a ciliary membrane contiguous with the plasma membrane. Between the basal body and the axoneme is the transition zone, which separates the ciliary membrane from the plasma membrane. Electron micrographs of the transition zone have identified Y-shaped densities, called Y-links, with the stem anchored at the microtubule doublets and the two arms attached to the ciliary membrane[6]. The components comprising the Y-links are unclear, as has been the arrangement of transition zone proteins.

Ciliopathies are diseases caused by defective ciliary function. Several ciliopathies are caused by mutations in genes encoding transition zone components[7,8]. *NPHP1* and *RPGRIP1L* are mutated in NPHP, characterized by kidney cysts[9,10]. Another subset of transition zone genes including *B9D1*, *TCTN2*, *TMEM231* and *RPGRIP1L,* are mutated in MKS, characterized by kidney cysts, polydactyly and occipital encephalocele. Mutations in many of these genes also cause JBTS, characterized by hypoplasia of the cerebellar vermis[11–18]. Consistent with their associations with different diseases, RPGRIP1L and NPHP1 are components of a protein complex called the NPHP complex, whereas B9D1, TCTN2 and TMEM231 are components of a distinct complex called the MKS complex[14,19,20]. In *C. elegans*, a homolog of RPGRIP1L is required for the transition zone localization of both the NPHP and MKS complexes[21,22]. Although how cilia transduce intercellular signals is becoming clearer, how JBTS-associated mutations affect ciliary functions remains obscure.

The transition zone controls the protein composition of the ciliary membrane. Genetic disruption of the transition zone in the mouse, *C. elegans*, or *C. reinhardtii* disrupts the ciliary localization of membrane-associated proteins[23–25]. For example, an essential mediator of the vertebrate Hedgehog signaling pathway, Smoothened (SMO), requires the transition zone proteins B9D1, TMEM231 and TCTN2 to accumulate within the ciliary membrane[14–16,20]. Consequently, loss of any of these proteins leads to Hedgehog-associated developmental defects[15,16,19].

Due to its critical role in regulating ciliary protein localization, the transition zone has been proposed to function as the gate to the cilium[26]. Understanding how it functions as a gate requires knowledge of its supra-molecular, sub-organellar structure. These structures are of sizes that can be resolved by super-resolution optical microscopy[27–30].

To elucidate the architecture of the ciliary gate, we combined two-color 3D STORM and quantitative image analysis[31,32]. We found that RPGRIP1L, TMEM231, NPHP1, and B9D1 form rings of differing diameters that lie outside the microtubule axoneme close to or at the ciliary membrane. These rings are comprised of discrete clusters spaced at non-uniform but non-random distances. Together with proximodistal measurements along the ciliary axis, we used diameter and radial distribution measurements to construct a three dimensional map of the transition zone at 15–30nm resolution, revealing that MKS and NPHP component localization is consistent with being at Y-links. Analysis of transition zone architecture in

human cells derived from JBTS-affected individuals indicated that RPGRIP1L and TCTN2 are essential for the localization of both the NPHP complex and the MKS complex. We found that SMO accumulates as a ring of discrete clusters specifically in the transition zone, suggesting that the transition zone is a point at which proteins pause on their way to or from the ciliary membrane. JBTS-associated *RPGRIP1L* mutations reduced the localization of SMO at the transition zone and the ciliary membrane, underscoring the importance of the transition zone for Hedgehog signaling. The approach to determining the relative three dimensional positions elucidated how ciliopathy mutations disrupt transition zone architecture and will be applicable to evaluating how other disease mutations compromise other sub-organellar assemblies.

RESULTS

NPHP and MKS complex components form discontinuous, concentric, nested rings within the transition zone

To assess differences in the arrangement of proteins associated with transition zone ciliopathies, we began by visualizing the transition zone of mouse tracheal epithelial cells (mTECs) using multicolor 3D Structured Illumination Microscopy (SIM). SIM revealed that mammalian NPHP1 was distributed in a ring in the transition zone of each cilium (Figure 1A).

We used single-color STORM to better resolve the distributions of ciliary proteins. The distal appendage protein CEP164 formed clusters arranged in a ring (Figure 1B), consistent with previous observations[28]. Interestingly, we found that the rings of the transition zone proteins RPGRIP1L, NPHP1, TMEM231, and B9D1 were also comprised of discrete clusters (Figures 1C–F).

Positioning a transition zone protein in a cylindrical coordinate system (with the *z*-axis along the cilium-axis) requires the determination of three coordinates: the radial distance from the ciliary axis, the angular position in the plane perpendicular to the axis, and the proximodistal position along the axis. For the first parameter, we measured the diameters of the transition zone rings (see Methods for details). Of the transition zone proteins assessed, TMEM231, a transmembrane protein likely to be part of the transition zone membrane[16], had the largest ring diameter (328±10nm, Figures 1C and 1G). RPGRIP1L ring had the smallest diameter (271±9nm, Figures 1D and 1G). The NPHP1 (283±12nm) and B9D1 (312±25nm) rings were intermediate (Figures 1E, 1F, and 1G). The distal appendage component CEP164 comprised a larger ring (404±30nm, Figures 1B and 1G). These measurements suggest that these transition zone proteins comprise concentric nested rings, with CEP164 in the distal appendages outside the transition zone, TMEM231 coincident with the transition zone membrane and B9D1, NPHP1, and RPGRIP1L rings positioned successively closer to the axoneme (Figure 1G).

The NPHP and MKS complexes form nine-fold symmetric doublets

Because transition zone protein rings were comprised of non-continuous clusters, we investigated whether these clusters were positioned randomly along the ring circumference.

Averaging CEP164 images indicated that it comprised 9 clusters symmetrically distributed around the ring (Figure 2A, right). In striking contrast, many TMEM231 and NPHP1 rings contained more than 9 clusters (Figures 1C and E), some of which were doublets oriented tangential to the ring circumference (yellow arrows in Figures 1C, E and F). Unlike CEP164, averaging NPHP1 or TMEM231 images did not reveal nine discrete clusters (Figures 2B Right, C Right and D Right), suggesting that the arrangement of transition zone proteins is more complex or heterogeneous than that of distal appendages.

To assess whether these clusters were randomly spaced, we generated an angular position histogram for each ring structure (Figures 2E–H) (see Methods for details). In nearest-cluster spacing analysis, A simulation of randomly position clusters resulted in evenly distributed angles between nearest clusters (Figure 2I), whereas nine symmetrically arranged clusters resulted in a peak at 40° (Figure 2J). The latter was close to the observed angle for CEP164 (peak position at 37°±2°, Figure 2E).

Consistent with the presence of more than nine NPHP1, TMEM231 and RPGRP1L clusters per ring, the angle between most of adjacent clusters was smaller than 40° (Figures 2F–H). Multi-Gaussian peak fitting of the histograms suggested that the angle distributions have three peaks (>80% of the boot-strapped histograms produced three peaks), two major peaks at ~14° and ~23°, and a minor peak at ~40°. This distribution paralleled that produced by a simulation of 9 symmetric doublets with one cluster unlabeled (Figure 2K). In this simulation, the intra-doublet and inter-doublet angles summed to 40° and produced the two major peaks, while the inter-doublet angles in which one cluster was unlabeled produced the minor peak at 40°. These results suggested that the transition zone is a wheel of nested rings, each comprised of nine symmetrically distributed doublets spaced approximately 23° from each other.

The observed doublets were reminiscent of ultrastructural features apparent in transmission electron micrographs (TEMs) of mouse ependymal cell transition zones (Figure 2L). These TEMs revealed densities called Y-links that span the microtubule doublets and the ciliary membrane in the shape of the letter Y (e.g., Figure 2L inside of dashed outline). The mean angle between the tips of Y-links was 20±2.3° (Figure 2L). Superimposing the STORM-based transition zone assembly onto the TEMs further highlighted the similarity between the MKS and NPHP complex localizations and the arms of the Y-links (Figure 2L).

NPHP1 and the MKS complex occupy the same proximodistal position in the transition zone

To map the third dimension of the transition zone model, we measured the axial positions along the ciliary axis. Using CEP164 as the common reference, we registered transition zone components with two-color 3D STORM (see Methods for details). Two-color 3D-STORM confirmed that the CEP164 ring is larger than the NPHP1 ring and revealed that the two rings are concentric (Figure 3A). Side views revealed that the NPHP1 ring is 122±36nm thick and 103±36nm distal to the CEP164 ring.

Similarly, we examined the axial position of the MKS complex components TMEM231 and B9D1. Two-color 3D STORM of CEP164 and either TMEM231 or B9D1 revealed that, like

NPHP1, TMEM231 and B9D1 rings are concentric with the CEP164 ring and 114±61 and 97±50nm thick, respectively (Figure 3B and C). Side views showed that the TMEM231 and B9D1 rings are 115±16nm and 91±40nm distal to CEP164, respectively (Figure 3B and C).

The similar distances of the NPHP complex member NPHP1 and the MKS complex member TMEM231 from CEP164 suggested that they are located in the same region along the ciliary proximodistal axis. Indeed, two-color 3D STORM of NPHP1 and TMEM231 confirmed that they are at the same proximodistal position along the cilium (Figure 3D).

Using the radial, angular and axial distributions of transition zone components, we generated a 3D model of the transition zone (Figure 3E). This model illustrates that the MKS and NPHP complexes are arranged as doublets arranged in concentric rings. These doublets are nine-fold symmetric, and likely to represent the arms of the Y-links connecting the ciliary membrane to the Y-link stem. The midpoints of the MKS and NPHP rings are ~110nm distal to the distal appendages, and the transition zone extends for ~120nm along the ciliary axis.

SMO and other ciliary proteins accumulate at the transition zone

The transition zone controls the composition of the ciliary membrane, as exemplified by SMO[33]. SMO accumulation in the cilium and subsequent Hedgehog pathway activation requires the transition zone MKS complex[14–16,20]. Hedgehog binding to its receptor, PTCH1, promotes the exit of PTCH1 from the cilium, and allows SMO to accumulate in the cilium[34,35]. Loss of PTCH1 leads to constitutive SMO localization to the cilium (as observed in *Ptch1*^{−/−} mouse embryonic fibroblasts [MEFs], Supplementary Figure S1) and constitutive pathway activation[36,37,38,39]. Recent single molecule studies have revealed that SMO pauses at an area near the ciliary base[40]. To determine where SMO localizes at the ciliary base, we visualized the position of SMO relative to the distal appendages and the transition zone using two-color SIM and 3D STORM. Wild-type unstimulated fibroblasts do not localize SMO to the ciliary membrane, as expected (Figure 3F). Wild-type fibroblasts treated with Smoothened Agonist (SAG)[41] showed SMO along the cilium with an accumulation at a region of the ciliary base distal to the distal appendages (Figure 3F). Similarly, *Ptch1*^{−/−} MEFs, in which Hedgehog signaling is active, displayed SMO along the cilium and accumulated near the base (Figure 3G, compared to wild type in Supplementary Figure S1).

To localize the accumulated SMO near the ciliary base, we examined the distribution of SMO and NPHP1 using two-color 3D STORM. We found that SMO largely colocalizes with NPHP1 (Figure 3G). Indeed, quantitation of SMO and NPHP1 along the ciliary axis indicated that SMO accumulates at the transition zone (Figure 3I).

Another protein that localizes to the ciliary membrane is ADCY3[42,43], a transmembrane adenylyl cyclase involved in olfaction, adiposity and male fertility[44–46]. Like SMO, ADCY3 accumulated at the transition zone (Figures 3H and I), suggesting that pausing at the transition zone may be a general characteristic of ciliary membrane proteins.

For comparison, we examined the localization of intraflagellar transport (IFT)-B complex component IFT88. IFT carries many ciliary proteins across the transition zone to the ciliary

tip. Consistent with previous indications that the IFT-B complex is assembled at the distal appendages[47], IFT88 prominently colocalized with CEP164 (Figure 3F). Another smaller accumulation of IFT88 was observed distal to the distal appendages (Figure 3F). Two-color 3D STORM confirmed that IFT88 predominantly localizes 110nm proximal to the transition zone, consistent with the distal appendages, with a second accumulation colocalizing with NPHP1 at the transition zone (Figures 3H and I). The enrichment of SMO, ADCY3 and IFT88 at the transition zone suggests that the transition zone is a waypoint at which diverse proteins entering or leaving the cilium pause.

JBTS-associated mutations in *TCTN2* disrupt MKS and NPHP complex localization to transition zone

Many of the more than 30 proteins associated with JBTS are components of the transition zone[26]. Mutations in *TCTN2* cause JBTS24[19], but understanding of how remains obscure. To assess how TCTN2 functions in the human transition zone, we examined how JBTS-associated compound heterozygous mutations in *TCTN2* affected the composition of the transition zone and ciliary membrane. The JBTS-affected individual is compound heterozygous for a missense mutation (G373R) and a frame shift mutation (D267fsX26) in *TCTN2*, whereas the two unaffected siblings are heterozygous for the missense mutation (G373R) and a wild type allele[48].

SIM and fluorescence intensity quantitation revealed that TCTN2 was reduced at the transition zone by 72±3% (mean difference±standard error of difference reported here and for subsequent fluorescence intensity measurements, Figure 4A). To begin to examine the consequences of loss of TCTN2 function, we assessed whether TCTN2 participates in the localization of TMEM231, another MKS complex protein underlying JBTS[11]. *TCTN2* mutant fibroblasts displayed a 75±5% reduction of TMEM231 at the transition zone (Figure 4A). Thus, human TCTN2 is required for the transition zone localization of TMEM231.

We further investigated whether *TCTN2* mutations affect the NPHP complex by assessing the localization of RPGRIP1L and NPHP1, two NPHP complex members mutated in JBTS[17,49]. *TCTN2* mutant fibroblasts displayed a 53±6% reduction of RPGRIP1L and 36±4% reduction of NPHP1 at the transition zone (Figure 4A). Thus, human TCTN2 is required to localize wild type amounts of both NPHP and MKS complex components at the transition zone.

In mice, the MKS complex is critical for the ciliary localization of ARL13B, a small GTPase[13]. As mutations in *ARL13B* also cause JBTS[50], we examined whether JBTS-associated mutations in *TCTN2* affect the ciliary localization of ARL13B. *TCTN2* mutant fibroblasts displayed a 37±5% reduction in ciliary ARL13B (Figure 4B). Thus, JBTS-associated mutations in *TCTN2* both disrupt the composition of the transition zone and diminish the ciliary localization of the JBTS-associated protein ARL13B.

NPHP1 has a subtle role in organizing the transition zone

To assess how NPHP1 functions in the transition zone, we examined how mutation of *Nphp1* in mouse embryonic fibroblasts affected the composition of the transition zone and ciliary membrane. SIM of *Nphp1*^{+/+} control and *Nphp1*^{−/−} fibroblasts revealed that, as

expected, NPHP1 was absent from the transition zone of $Nphp1^{-/-}$ cells (100±8%, Figure 4C). To examine the consequences of loss of NPHP1 function, we assessed whether NPHP1 participates in the localization of RPGRIP1L. We found that RPGRIP1L was reduced by 15±6% from the transition zones of $Nphp1^{-/-}$ cells (Figure 4C). Thus, NPHP1 has a minor role in the transition zone localization of RPGRIP1L.

We further investigated whether NPHP1 organizes the MKS complex by assessing the localization of TMEM231. The quantity of TMEM231 in the transition zone was unaffected in $Nphp1^{-/-}$ cells (4±7%, Figure 4C). Thus, NPHP1 is not required for the transition zone localization of a key MKS complex component.

We also examined whether NPHP1 participates in the ciliary localization of ARL13B. Surprisingly, ARL13B levels were elevated by 20±4% in $Nphp1^{-/-}$ cells (Figure 4D). Thus, whereas NPHP1 has a minor role in the localization of another NPHP component, RPGRIP1L, to the transition zone, it is dispensable for localization of one MKS component and dispensable for the MKS complex-dependent localization of ARL13B to the cilium.

JBTS mutations in *RPGRIP1L* displace MKS and NHP complex proteins from the transition zone

To assess human RPGRIP1L function, we examined how JBTS-associated compound heterozygous mutations of three individuals from two families affected the transition zone and ciliary composition. The JBTS-affected individuals have missense mutations affecting the C2-N domain of RPGRIP1L in combination with a nonsense mutation (Supplementary Figure S2)[48]. SIM and fluorescence intensity quantitation of control fibroblasts from an unaffected sibling and three affected individuals revealed that the JBTS-associated mutations in *RPGRIP1L* reduced the level of RPGRIP1L at the transition zone by 81±3% (Figure 5A). To examine the consequences of loss of RPGRIP1L function, we assessed the localization of NPHP1 and found that NPHP1 was reduced by 85±7% from the *RPGRIP1L* mutant transition zone (Figure 5A). Thus, whereas NPHP1 has only a minor role in localizing RPGRIP1L to the transition zone (Figure 4C), RPGRIP1L has a major role in localizing NPHP1.

We further investigated whether *RPGRIP1L* mutations affect the MKS complex components TMEM231 and TCTN2. TCTN2 and TMEM231 were both reduced within the transition zones of *RPGRIP1L* mutant cells (TCTN2 was reduced 56±5%; TMEM231 was reduced 62±5%, Figure 5A). Thus, human RPGRIP1L is required for the transition zone localization of both NPHP1 and MKS complex components.

In addition to *RPGRIP1L* and *NPHP1*, mutations in *AHI1* cause JBTS[51,52]. We therefore examined whether RPGRIP1L affects the transition zone localization of AHI1. Like NPHP1, TCTN2 and TMEM231, established components of the NPHP and MKS complexes, AHI1 localized predominantly at the transition zone in a way that depended on RPGRIP1L (65±6% reduction, Figure 5A).

To assess transition zone function, we examined whether *RPGRIP1L* affects the ciliary localization of ARL13B. ARL13B levels were reduced by 49±6% in *RPGRIP1L* mutant

fibroblasts (Figure 5B). Thus, not only does JBTS-associated mutations in *TCTN2* (Figure 4A) disrupt the composition of the transition zone, JBTS-associated mutation of *RPGRIP1L* does as well, and both proteins are required to promote the ciliary localization of the JBTS-associated protein ARL13B.

Mutation of mouse *Rpgrip1l* leads to altered Hedgehog signaling[53]. As RPGRIP1L is required for the organization of the transition zone and the transition zone is a waypoint for SMO entering or leaving the cilium, we hypothesized that JBTS-associated mutations affect SMO localization to cilia. To test this hypothesis, we stimulated cells with SAG and assessed SMO localization. In wild type human fibroblasts, SMO localized to cilia in a SAG-dependent manner, as expected (Figure 5C). In contrast, SAG only poorly stimulated the ciliary localization of SMO in *RPGRIP1L* mutant fibroblasts; ciliary SMO levels were reduced by $78 \pm 9\%$, Figure 5C). Moreover, SMO did not accumulate in the transition zones of SAG-stimulated *RPGRIP1L* mutant fibroblasts (Figure 5C). Thus, JBTS-associated mutations in *RPGRIP1L* disrupt the composition of the transition zone, diminishing the ciliary localization of essential developmental regulators such as ARL13B and SMO.

JBTS mutations in *RPGRIP1L* disrupt transition zone architecture

To further assess how RPGRIP1L functions in the human transition zone, we examined how JBTS-associated mutations in *RPGRIP1L* affected transition zone organization and function using 3D STORM. Mutations in *RPGRIP1L* disrupted both the RPGRIP1L and NPHP1 transition zone rings (Figure 6A). In addition, STORM revealed that, although TCTN2 levels in the transition zone were reduced (Figure 5A), the remaining TCTN2 formed a ring (Figure 6A). Thus, RPGRIP1L regulates the quantity of TCTN2 in the transition zone, but the organization of TCTN2 into a ring does not depend critically on RPGRIP1L. In contrast, the TMEM231 ring was lost from the transition zones of *RPGRIP1L* mutant cells (Figure 6A). Thus, human RPGRIP1L organizes both the NPHP1 and TMEM231 rings, but the TCTN2 ring is less dependent on RPGRIP1L.

STORM revealed that, in control fibroblasts, ARL13B is present throughout the ciliary membrane and as a ring in the transition zone (Figure 6B). In *RPGRIP1L* mutant cells, the transition zone ring of ARL13B was present but ARL13B was reduced in the cilium (Figure 6B). Thus, JBTS-associated mutation of *RPGRIP1L* only partially disrupts the function of the transition zone as a ciliary waypoint.

STORM of control fibroblasts confirmed that SAG stimulated the accumulation of SMO within cilia and within a ring of the transition zone (Figure 6C). In contrast, SMO failed to accumulate in the cilium or transition zone of *RPGRIP1L* mutant fibroblasts (Figure 6C). Thus, JBTS-associated mutations in *RPGRIP1L* disrupt the composition and architecture of the transition zone, diminishing the levels and impairing the organization of ciliary membrane proteins, such as ARL13B and SMO. We propose that some forms of JBTS are transition zone-opathies whose phenotypes are due to compromised ciliary signaling secondary to disruption of transition zone architecture.

DISCUSSION

Structural mapping by super-resolution microscopy reveals that JBTS-associated proteins form nested rings of doublets in the transition zone

Super-resolution microscopy has emerged as a powerful tool for analyzing the molecular organization of large protein complexes[27,30,54–56]. Key to this approach is determining the relative position of complex components. Calculation of positional coordinates enables 3D rendering of a complex or, in our case, a sub-organellar compartment. Here, we have demonstrated mapping of the ciliary base by analyzing the radial, angular and axial distribution of its components. Both the imaging and analysis methods used here can be readily applied to other structural mapping efforts.

By determining the arrangement of key ciliopathy-associated proteins in the transition zone, we found that the MKS and NPHP complexes form nested rings, with the MKS complex positioned at the transition zone membrane and the NPHP complex positioned within the MKS complex closer to the ciliary axoneme. Both of the NPHP and MKS complexes form nine-fold doublets, similar to the doublets represented by the arms of the Y-links..

Our finding that JBTS-causing mutations in *RPGRIP1L* and *TCTN2* disrupt both the NPHP and MKS complexes in the transition zone reveals a structural basis for the functional interactions that have been observed between the two complexes. For example, in mice, compound mutation of genes encoding MKS and NPHP complex components synergistically disrupts ciliogenesis and Hedgehog developmental signaling[57]. Similarly, in *C. elegans,* mutation of individual MKS or NPHP complex genes does not disrupt ciliogenesis, but compound mutation of MKS and NPHP complex genes abrogate ciliary structure[22,57]. The overlapping localizations and functions of the NPHP and MKS complexes suggest that they have partially overlapping roles in controlling ciliogenesis and ciliary composition (Figure 6D). Our structural analysis suggests that this functional overlap may reflect partially interdependent generation of the transition zone super-assembly by the MKS and NPHP complexes.

The transition zone is a waypoint for diverse ciliary proteins

The transition zone acts as a gate that accumulates some proteins within the cilium, either by facilitating ciliary entry or preventing ciliary exit, and restricts the entrance of others. This gating is essential for Hedgehog signaling-induced SMO accumulation in cilia and vertebrate development[58]. We found that ADCY3 and, upon activation of the Hedgehog pathway, SMO accumulate at discrete clusters within the transition zone. Single-molecule imaging has shown that SMO pauses in the vicinity of the ciliary base[40]. Based on two-color STORM data, we propose that these pauses occur in the transition zone. As SMO localization to the transition zone requires RPGRIP1L, either RPGRIP1L itself or RPGRIP1L-dependent proteins are likely to be SMO binding sites. This transient accumulation in the transition zone suggests that the MKS complex acts as a waypoint for SMO promoting its entry into or preventing its exit from the cilium.

Why might ciliary proteins pause at the transition zone? One possibility is that the transition zone is the place where ciliary cargo is loaded onto the IFT machinery entering the cilium.

Consistent with this model of cargo loading at the transition zone, IFT88 also accumulated at the transition zone (Figures 3H and I).

Transition zone disruption is a cause of Joubert syndrome

The involvement of ciliary proteins in both Hedgehog signaling and JBTS suggests that disruptions in Hedgehog signaling may underlie JBTS[59,60]. Our data reveal that mutations in *TCTN2* that cause JBTS disrupt the localization of other JBTS-associated transition zone proteins including NPHP1, RPGRIP1L, and TMEM231. Moreover, mutations in human *RPGRIP1L* that cause JBTS disrupt the localization of JBTS-associated transition zone proteins NPHP1, TCTN2, TMEM231 and AHI1. Still other JBTS-associated transition zone proteins (*e.g.*, CEP290) may also depend on TCTN2 and RPGRIP1L for localization.

The requirement for human RPGRIP1L in localizing both NPHP and MKS components parallels the requirement for a RPGRIP1L homolog, MKS-5, in *C. elegans*[21,22]. Thus, RPGRIP1L is a core organizer of the transition zone whose functions are evolutionarily conserved from nematodes to humans. In contrast, the sole member of the *C. elegans* Tectonic family is dispensable for MKS-5 transition zone localization[57], indicating that evolution has altered the functions of other transition zone components.

We previously reported that mouse MKS complex components control the ciliary localization of SMO, and are required for Hedgehog signaling[14,19]. Here, we found that, like the MKS complex, human RPGRIP1L is essential for SMO accumulation at the cilium in response to pathway activation. It is likely that RPGRIP1L, by organizing the MKS complex at the transition zone, is required for SMO to accumulate in cilia and activate the downstream Hedgehog pathway.

Unlike most JBTS-associated proteins, ARL13B localizes to the ciliary membrane. TCTN2 and RPGRIP1L are essential for ARL13B localization to cilia. Thus, the diverse genes underlying JBTS may fall into one of at least three categories: 1) genes, such as *TCTN2* and *RPGRIP1L*, required to organize the transition zone, 2) genes, such as *NPHP1*, that are not essential for transition zone organization but contribute to its function, and 3) genes, such as *ARL13B*, that encode proteins that are localized to cilia by the transition zone. The transition zone super-assembly is critical for the ciliary localization of proteins of this third category, and perturbation of its architecture is thus a cause of JBTS.

METHODS

Primary mouse tracheal epithelial cell culture

Primary mouse tracheal epithelial cultures were derived as described[61]. In summary, tracheas from C57BL/6J mice aged 8 to 12 weeks were dissected. The tracheal cells were dissociated with protease. Dissociated cells were placed in a culture plate (Primaria) for several hours to remove fibroblasts. The non-adherent tracheal epithelial cells were seeded at a density of 0.33×10^5 cells per 24-well insert (Day 0). The cells were cultured for three days with mTEC/Plus medium in the basal and apical compartments of the transwell. After three days of incubation (Day 3), the medium was replaced with fresh mTEC/Plus medium. Air-liquid interface (ALI) differentiation was begun at day 5 by removing the medium in the

apical transwell chamber and replacing the medium in the basal chamber with mTEC/NS. The medium was replaced every other day with mTEC/NS, and the filters were harvested at ALI day 14 for immunofluorescence experiments. All animal protocols were approved by the Institutional Animal Care and Use Committee (IACUC) of the University of California, San Francisco.

IMCD3 and fibroblast cell culture

IMCD3 cells were cultured in DMEM:F12 supplemented with 10% FBS. MEFs and human primary dermal fibroblasts were cultured in DMEM, Glutamax (Thermo Fisher), and 10% FBS. For imaging, IMCD3 cells, MEFs, and human primary dermal fibroblasts were seeded at 2.5×10^4 cells/cm^2 and grown to confluency. Cells were starved of serum in Opti-MEM reduced serum medium for 24 hours to induce ciliogenesis. Cell lines were not authenticated. No commonly misidentified cell lines were used. All growing cell lines were routinely tested for mycoplasma.

Fixation and staining for immunofluorescence

mTEC filters were harvested at ALI day 14 and the apical and basal compartments were washed with phosphate buffered saline (PBS) three times. The filters were fixed by adding 4% paraformaldehyde (PFA) in PBS to the apical compartment and incubating at room temperature for ten minutes. The PFA was removed by washing the filter with PBS six times with at least one minute of incubation between washes. The filters were then treated with a solution of 1% sodium dodecyl sulfate (SDS) for five minutes in PBS to reveal antigens. The SDS solution was removed by washing the filter with PBS.

For SIM, filters were incubated in blocking buffer (PBS, 2.5 % BSA, 0.1 % Triton X-100, 0.02 % sodium azide) for ten minutes at room temperature. Primary antibodies were added to the filters in blocking buffer according as described in Supplementary Table S1. The filters were incubated overnight (~16 hours) at 4 degrees on a rocker. The filters were washed with PBT (PBS, 0.2% Triton X-100) six times with at least one minute of incubation between washes. Secondary antibodies were added at a dilution of 1:1000 and incubated for two hours in blocking buffer on an orbital shaker. The secondary antibody was removed by six washes with PBT buffer. The filters were mounted on slides in Prolong Gold containing 4′,6-diamidino-2-phenylindole (DAPI). High performance coverslips were used, and the mounting medium was allowed to solidify for 16–24 hours before sealing the slides with nail polish and imaging.

For STORM, filters were incubated in blocking buffer for ten minutes at room temperature. Primary antibodies were added to the filters incubating in blocking buffer according to the table of antibodies and concentrations (Table 1). The filters were incubated with the primary antibody overnight (~16 hours) at 4 °C on a rocker. The filter was washed with PBT. Secondary antibodies were incubated for two hours at room temperature or overnight (~16 hours) at 4 °C on the filters in blocking buffer. The secondary antibody was removed by six washes with PBT.

Some samples for single color STORM were stained using labeled primary antibodies. In these cases, filters were incubated in blocking buffer for ten minutes at room temperature.

Primary antibodies were added to the filters in blocking buffer at concentrations listed in Table 1. The filters were incubated with the primary antibody overnight (~16 hours) at 4 °C on a rocker. The filter was washed with PBT.

For two-color STORM using primaries derived from the same species, filters were incubated in IF blocking buffer for ten minutes at room temperature. Primary antibody recognizing the experimental protein was added to the filters incubating in blocking buffer. The filters were incubated with the primary antibody overnight (~16 hours) at 4 °C on a laboratory rocker. The filter was washed with PBT. Secondary antibody labelled with Alexa 647 was added according to the table and incubated for two hours at room temperature on the filters in IF blocking buffer. The secondary antibody was removed by six washes with Wash buffer. Primary antibody labelled with Cy5.5 recognizing the reference protein was added to the filters incubating in blocking buffer according to the table of antibodies and concentrations. The filters were incubated with the primary antibody overnight (~16 hours) at 4 °C on a laboratory rocker. The filter was washed with PBT. All antibody information is available in Supplementary Table 1

Mounting filters in STORM buffer

After immunofluorescence staining, mTEC filters were mounted on slides and high-performance coverslips in PBS with the addition of 100 mM mercaptoethylamine at pH 8.5, 5% glucose (wt/vol) and oxygen scavenging enzymes [0.5 mg/ml glucose oxidase (Sigma-Aldrich), and 40 mg/ml catalase (Roche Applied Science)]. The buffer remains suitable for imaging for two hours.

SIM image acquisition

SIM data were collected on a N-SIM microscope in 3D-SIM mode using an Apo TIRF 100x oil NA 1.49 objective (Nikon) following standard operation procedures. Image reconstruction was using the NIS Elements software (Nikon).

STORM instrumentation

STORM experiments were performed on a custom-built microscope based on a Nikon Ti-U inverted microscope. Three activation/imaging photodiode lasers (Coherent CUBE 405, OBIS 561 and CUBE 642) were combined using dichroic mirrors, aligned, expanded and focused to the back focal plane of the objective (Nikon Plan Apo 100x oil NA 1.45). The lasers were controlled directly by the computer. A quadband dichroic mirror (zt405/488/561/640rpc, Chroma) and a band-pass filter (ET705/70m, Chroma) separated the fluorescence emission from the excitation light. The focus drift of the microscope sample stage during image acquisition was stabilized by a closed-loop focus stabilization system that sends an infra-red laser beam through the edge of the microscope objective and detects the back reflection from the sample coverglass with a CCD camera[32].

After the emission light exits the microscope side port, we added a low-end piezoelectric deformable mirror (DM) (DMP40-P01, Thorlabs) at the conjugate plane of the objective pupil plane. This DM contains 40 actuators arranged in a circular keystone pattern. By first flattening the mirror and then manually adjusting key Zernike polynomials of the DM

surface, we found that this DM has sufficient performance to correct aberrations induced by the optical system. We did not observe obvious depth-induced spherical aberrations caused by glass-water refractive index mismatch because transition zones we imaged were < 1 μm away from the coverglass surface. Moreover, after correcting the intrinsic aberrations, we increased the primary astigmatism Zernike coefficient of the DM surface to introduce astigmatism for 3D STORM. To experimentally generate a calibration curve of point spread function as a function of z, we immobilized Alexa 647–labeled antibodies on a coverglass and imaged individual molecules as the sample was scanned in z[32]. Compared to using a cylindrical lens[32] using the DM to introduce astigmatism did not cause magnification differences in the two lateral directions. It also allowed tractable optimization of the amount of astigmatism to achieve the best axial resolution. The Z localization precision (Z resolution) is estimated to be ~70nm full width at half maximum (FWHM) based on the reconstructed STORM images. The Z focal depth is ~800 nm. We measured the longitudinal distance between the transition zone and distal appendages by analyzing only transition zone structures with their axes close to the XY plane. Therefore, the precision was limited mostly by the XY resolution instead of Z resolution.

The fluorescence was subsequently split by a 705nm beam splitter (T705lpxr, Chroma) to a long wavelength channel (ch1, >705 nm) and a short wavelength channel (ch2, <705 nm). The two channels were recorded at a frame rate of 57 Hz on an electron multiplying CCD camera (Ixon+ DU897E-CS0-BV, Andor). The split-view setup discriminates fluorescent labeled by small shifts (~20nm) in their emission spectra, in this work Alexa Fluor 647 and Cy5.5. Because individual emitters were recorded in both long and short channels, the intensity ratio between the channels is sufficient to identify each emitter[62].

STORM image acquisition and analysis

Photoswitchable dye pairs Alexa 405/Alexa 647 and Cy3/Cy5.5 were used for STORM imaging with a ratio of 0.8 Alexa 647 molecules per antibody, and 0.5 Cy5.5 per antibody. During the imaging process, the 405nm and 561nm activation lasers were used to activate a small fraction of the Alexa 647 and Cy5.5 reporters at a time, and individual activated fluorophores were excited with a 642nm laser. The typical power for the lasers at the back port of the microscope was 30 mW for the 642nm imaging laser and 0.5 to 5 μW for activation lasers.

Analysis of STORM raw data was performed in the Insight3 software[32], which identifies and fits single molecule spots in each camera frame to determine their x, y and z coordinates as well as photon numbers. Sample drift during data acquisition were corrected using imaging correlation analysis. The drift-corrected coordinates, photon number, and the frame of appearance of each identified molecule were saved in a molecule list for further analysis.

To estimate position uncertainty, we considered several factors. First, we measured single-molecule localization precision in our images to be ~15nm (SD) by analyzing the relative position of the same photoactivated molecule appearing in consecutive frames. Second, the antibody size contributed additional error. Previous STORM of indirectly immunostained microtubules revealed that primary and secondary antibodies adds ~30nm to the overall diameter[34], suggesting a localization bias up to 15nm in cases in which primary and

secondary antibodies bind from a uniform direction. Given that we used polyclonal antibodies of all TZ targets, we did not anticipate biased binding orientation to occur. When the orientation of antibody binding is random, combining the 15nm localization precision and a 30nm uniform distribution from the antibodies (SD = 9nm) results in an overall uncertainty of 17nm (SD).

Ratiometric color identification and self-referenced registration

Because of the high labeling density for transition zone proteins, multi-color STORM utilizing activator-reporter dye pairs with different activation wavelengths[31] suffer from high cross-talk between color channels. Therefore, we choose to use reporter dyes with distinct emission spectra for two-color imaging. Typically, this approach uses a dichroic mirror to split the emission light into two distinct channels, most commonly two halves of the same camera chip. The drawback, though, is that the two channels must be registered with nanometer accuracy. This registration requires additional calibration images acquired before every imaging experiment (e.g. using fluorescent beads). Moreover, three-dimensional channel registration could be complicated due to the chromatic aberrations between channels.

To overcome these inconveniences, we purposely used two reporter dyes which have substantial overlap in the emission spectra. We chose far-red photoswitchable cyanine dyes Alexa Fluo 647 and Cy5.5 because they have superior photoswitching characteristics than most shorter-wavelength dyes. In our system, approximately 60% of Alexa 647 emission and 48% of Cy5.5 emission went into the shorter wavelength channel and the rest into the longer wavelength channel. Because the same Cy5.5 molecule appears in both channels with approximately equal intensity, the STORM data itself contains channel registration information. We extracted this information by first manually identifying 3–4 pairs matched spots in the two channels to calculate crude registration information, then automatically identify all matched spots in ~ 1000 STORM frames using this crude registration information, and finally determine a polynomial coordinate transform function between the two channels with a least square fitting to the coordinates of these matched spots. The least square fitting can be performed for just the xy coordinates or for all xyz coordinates. In this work, we only performed 2D registration for the subsequent determination of color identity. The polynomial transform function is: $x_c = A_0 + A_1 x + B_1 y + A_2 x^2 + C_2 x y + B_2 y^2 + A_3 x^3 + C_{31} x y^2 + C_{32} x^2 y + B_3 y^3$; $y_c = E_0 + E_1 y + F_1 x + E_2 y^2 + G_2 x y + F_2 x^2 + E_3 y^3 + G_{32} x^2 y + G_{31} x y^2 + F_3 x^3$; where x_c and y_c are the transformed coordinates, x and y are the initial coordinates, and A_0, A_1, A_2, A_3, B_1, B_2, B_3, C_2, C_{31}, C_{32}, E_0, E_1, E_2, E_3, F_1, F_2, F_3, G_2, G_{31}, and G_{32} are coefficients obtained by the least square fitting.

With the 2D registration information, all spots identified in the short wavelength channel (containing both Alexa 647 and Cy5.5) were mapped to the longer wavelength cannel to calculate the corresponding intensity. The color identity of each single molecule spot was then determined based on the intensities in the two channels, I_S and I_L. Using samples labeled with only one of the two dyes, we generated a calibration plot in the $\log(I_S)$-$\log(I_L)$ representation, with areas corresponding to the two dyes cleanly separated by a straight line. The crosstalk between the two channels is approximately 15%.

To construct the final super-resolution image, we used the coordinate information from only the shorter wavelength channel so that the two colors are perfectly aligned without chromatic aberration. Although this approach sacrifices spatial resolution because some of the emission photons are in the longer wavelength detection channel, we found that the final spatial resolution was sufficient for our study. In applications demanding better spatial resolution, it would be straightforward to merge the positional information from both channels utilizing the channel registration information extracted from the STORM data itself.

Diameter measurement

We robust-fitted each ring structure imaged by STORM to an ellipse[63]. We chose robust fit instead of least square fit to avoid outlier effects from noise localization points in the STORM image. The diameter of a circle with the same perimeter of the ellipse was considered as the diameter of its corresponding structure. The diameter of structure formed by each kind of protein was determined by averaging about 30 fitted structures. The proteins we measured were NPHP1, TEM231, B9D1 and RPGRIP1L in the transition zone, and CEP164 in distal appendages.

Image alignment using discrete Fourier transform (DFT) and cross correlation

The alignment algorithm is a modified version of image registration[64] that achieved efficient subpixel image registration by upsampled DFT cross correlation and takes into account sample rotation. Briefly, the original algorithm (1) obtains an initial 2D shift estimate of the cross correlation peak by fast Fourier transforming (FFT) a image to register and a reference image, (2) and then refines the shift estimation by upsampling the DFT only in a small neighborhood of that estimate by means of a matrix-multiply DFT. We modified step (1) by rotating the image to align from 0 to 359° by 1° at a step, and then performing original step (1) after each rotation step to obtain 360 cross correlation peaks. The biggest peak provides not only the initial 2D shift estimate but also the optimal angle of rotation. The initial 2D shift estimate then goes through the same step (2) in the original algorism to achieve subpixel alignment. The images of single structure were aligned for 10 iterations. The superimposition of all images was used as the reference image for the first iteration. Each image was translated and rotated to the reference image to maximize the cross correlation between the image to align and reference image in Fourier domain. The superimposition of the images aligned in one iteration was used as the reference image for the next iteration. Our algorithm aligned the images within 1/100 of a pixel.

Nearest-cluster angular spacing analysis and bootstrapping

The nearest-cluster angular spacing analysis is based on the coordinates in STORM images. To analyze the angles between nearest clusters in the transition zone protein and CEP164 rings, we (1) fitted each structure to a ring, converted the Cartesian coordinates to polar coordinates, and constructed a histogram of the angles of all localizations in each STORM image, (2) found the peaks in the histogram with multiple Gaussian functions using a matlab program findpeaksb.m developed by Dr. T. C. O'Haver at Univeristy of Maryland (https://terpconnect.umd.edu/~toh/spectrum/PeakFindingandMeasurement.htm), (3) calculated the angle between nearest peaks, (4) plotted a histogram of the central angles between nearest

peaks (clusters) obtained from n individual images (n = 50~125), and finally (5) found the peaks in the histogram of nearest-cluster angular spacing by fitting them to multiple Gaussian functions using findpeaksb.m (Figure 2E–H). The positions of the centers of the fitted Gaussian functions obtained in step (5) were used as the angles between adjacent clusters in the model of TZ architecture (Figure 2E–H). The uncertainties of these angles were estimated by bootstrapping analysis. This technique allows estimation of the sampling distribution by random sampling the individual images to new sets of images. Each new set has the same number of images as in the original set. We randomly sampled 200 sets of images for each protein in our bootstrapping analysis to test the robustness of peak identification and calculate the standard deviation of nearest-cluster angles. For TZ proteins NPHP1, TMEM231, B9D1, and RPGRIP1L, more than 80% of the bootstrapping histograms of nearest-cluster angles have three peaks as demonstrated in Figures 2E–H.

The findpeaksb.m program determines the number of peaks and the position, width and height of each peak by least-squares curve-fitting to the original histograms. More specifically, it smooths the first derivative of the histogram, detects downward-going zero-crossings, and takes only those zero crossings whose slope exceeds a certain predetermined minimum (called the slope threshold) t a point where the original signal exceeds a certain minimum (called the amplitude threshold"). We set the smooth width, slope threshold, and amplitude threshold for the algorithm, and kept these parameters constant for CEP164 (Figure 2E) and transition zone proteins (Figure 2F–H).

Quantitation of fluorescence intensity in human fibroblasts

Confocal images of cilia were collected on a Leica SPE laser-scanning confocal equipped with four laser lines (405nm, 488nm, 551nm, and 635nm) and an ACS APO 63x/1.30 NA oil objective lens. The fluorescence intensity of individual cilia and transition zones in confocal micrographs was measured using Fiji software[65]. The average background fluorescence intensity in the vicinity of each transition zone and cilium was subtracted from the fluorescence intensity of individual transition zones and cilia.

Structural homology modeling

Homology models were generated using ModWeb version r182[66,67].

Domain architecture prediction

Domain architecture predications were generated using JPred 4 and Topcons web servers[68,69].

Human research subjects

Informed consent was obtained from all research participants or their legal guardians, and all research procedures were performed in compliance with a human research protocol approved by the Institutional Review Board at the University of Washington. Specific information on each patient is provided in Supplementary Table 3.

Code availability

Custom-written image analysis software is available from the corresponding authors on request.

Statistics and reproducibility

Statistical analyses were performed using Graphpad Prism 7.0a. Graphical data are presented as mean±95% confidence interval or mean±standard deviation as specified in the figure legends. n values are stated in the figure legends and definition of n is number of transition zones (Figures 4A, 4C, and 5A) or number of cilia (Figures 4B, 4D, 5B, and 5C). P values are stated in the figure legends, and symbols indicate the following P values: ns, P > 0.05. *, P 0.05. **, P 0.01. ***, P 0.001. ****, P 0.0001. Two sample comparisons were performed using an unpaired t test with a two tailed P value. Multiple comparisons were performed using an ordinary one-way ANOVA, along with Tukey's multiple comparisons test to analyze pairwise differences. Fluorescence intensity measurements (Figures 4 and 5) from multiple experiments were combined for statistical analysis. Negative normalized fluorescence intensity values were set to zero in graphs. Experiments were independently performed either twice (Figures 4A, 4B, and 5C) or thrice (Figure 1G, 2E–H, 4C, 5A, and 5B).

Data availability statement

Source data for experiments in figures 4 and 5 are provided in Supplementary Table 2. All other data supporting the findings of this study are available from the corresponding authors on reasonable request.

Supplementary Material

Refer to Web version on PubMed Central for supplementary material.

Acknowledgments

References

1. Dutcher SK. The awesome power of dikaryons for studying flagella and basal bodies in Chlamydomonas reinhardtii. Cytoskeleton (Hoboken). 2014; 71:79–94. [PubMed: 24272949]

2. Pearson CG, Winey M. Basal body assembly in ciliates: the power of numbers. Traffic. 2009; 10:461–471. [PubMed: 19192246]

3. Garcia G, Reiter JF. A primer on the mouse basal body. Cilia. 2016; 5:17. [PubMed: 27114821]

4. Vertii A, Hung HF, Hehnly H, Doxsey S. Human basal body basics. Cilia. 2016; 5:13. [PubMed: 26981235]

5. Anderson RG. The three-dimensional structure of the basal body from the rhesus monkey oviduct. J Cell Biol. 1972; 54:246–265. [PubMed: 5064817]

6. Gilula NB, Satir P. The ciliary necklace. A ciliary membrane specialization. J Cell Biol. 1972; 53:494–509. [PubMed: 4554367]

7. Habbig S, Liebau MC. Ciliopathies - from rare inherited cystic kidney diseases to basic cellular function. Mol Cell Pediatr. 2015; 2:8. [PubMed: 26542298]

8. Szymanska K, Hartill VL, Johnson CA. Unraveling the genetics of Joubert and Meckel-Gruber syndromes. J Pediatr Genet. 2014; 3:65–78. [PubMed: 25729630]

9. Otto E, et al. A gene mutated in nephronophthisis and retinitis pigmentosa encodes a novel protein, nephroretinin, conserved in evolution. Am J Hum Genet. 2002; 71:1161–1167. [PubMed: 12205563]

10. Wolf MTF, et al. Mutational analysis of the RPGRIP1L gene in patients with Joubert syndrome and nephronophthisis. Kidney Int. 2007; 72:1520–1526. [PubMed: 17960139]

11. Srour M, et al. Mutations in TMEM231 cause Joubert syndrome in French Canadians. J Med Genet. 2012; 49:636–641. [PubMed: 23012439]

12. Arts HH, et al. Mutations in the gene encoding the basal body protein RPGRIP1L, a nephrocystin-4 interactor, cause Joubert syndrome. Nat Genet. 2007; 39:882–888. [PubMed: 17558407]

13. Hopp K, et al. B9D1 is revealed as a novel Meckel syndrome (MKS) gene by targeted exon-enriched next-generation sequencing and deletion analysis. Hum Mol Genet. 2011; 20:2524–2534. [PubMed: 21493627]

14. Garcia-Gonzalo FR, et al. A transition zone complex regulates mammalian ciliogenesis and ciliary membrane composition. Nat Genet. 2011; 43:776–784. [PubMed: 21725307]

15. Dowdle WE, et al. Disruption of a ciliary B9 protein complex causes Meckel syndrome. Am J Hum Genet. 2011; 89:94–110. [PubMed: 21763481]

16. Roberson EC, et al. TMEM231, mutated in orofaciodigital and Meckel syndromes, organizes the ciliary transition zone. J Cell Biol. 2015; 209:129–142. [PubMed: 25869670]

17. Delous M, et al. The ciliary gene RPGRIP1L is mutated in cerebello-oculo-renal syndrome (Joubert syndrome type B) and Meckel syndrome. Nat Genet. 2007; 39:875–881. [PubMed: 17558409]

18. Joubert M, Eisenring JJ, Robb JP, Andermann F. Familial agenesis of the cerebellar vermis. A syndrome of episodic hyperpnea, abnormal eye movements, ataxia, and retardation. Neurology. 1969; 19:813–825. [PubMed: 5816874]

19. Sang L, et al. Mapping the NPHP-JBTS-MKS protein network reveals ciliopathy disease genes and pathways. Cell. 2011; 145:513–528. [PubMed: 21565611]

20. Chih B, et al. A ciliopathy complex at the transition zone protects the cilia as a privileged membrane domain. Nat Cell Biol. 2012; 14:61–72.

21. Jensen VL, et al. Formation of the transition zone by Mks5/Rpgrip1L establishes a ciliary zone of exclusion (CIZE) that compartmentalises ciliary signalling proteins and controls PIP2 ciliary abundance. EMBO J. 2015; 34:2537–2556. [PubMed: 26392567]

22. Williams CL, et al. MKS and NPHP modules cooperate to establish basal body/transition zone membrane associations and ciliary gate function during ciliogenesis. J Cell Biol. 2011; 192:1023–1041. [PubMed: 21422230]

23. Reiter JF, Blacque OE, Leroux MR. The base of the cilium: roles for transition fibres and the transition zone in ciliary formation, maintenance and compartmentalization. EMBO Rep. 2012; 13:608–618. [PubMed: 22653444]

24. Awata J, et al. NPHP4 controls ciliary trafficking of membrane proteins and large soluble proteins at the transition zone. J Cell Sci. 2014; 127:4714–4727. [PubMed: 25150219]

25. Craige B, et al. CEP290 tethers flagellar transition zone microtubules to the membrane and regulates flagellar protein content. J Cell Biol. 2010; 190:927–940. [PubMed: 20819941]

26. Garcia-Gonzalo FR, Reiter JF. Scoring a backstage pass: mechanisms of ciliogenesis and ciliary access. J Cell Biol. 2012; 197:697–709. [PubMed: 22689651]

27. Mennella V, et al. Subdiffraction-resolution fluorescence microscopy reveals a domain of the centrosome critical for pericentriolar material organization. Nat Cell Biol. 2012; 14:1159–1168. [PubMed: 23086239]

28. Lau L, Lee YL, Sahl SJ, Stearns T, Moerner WE. STED microscopy with optimized labeling density reveals 9-fold arrangement of a centriole protein. Biophys J. 2012; 102:2926–2935. [PubMed: 22735543]

29. Yang TT, et al. Superresolution Pattern Recognition Reveals the Architectural Map of the Ciliary Transition Zone. Sci Rep. 2015; 5:14096. [PubMed: 26365165]

30. Lawo S, Hasegan M, Gupta GD, Pelletier L. Subdiffraction imaging of centrosomes reveals higher-order organizational features of pericentriolar material. Nat Cell Biol. 2012; 14:1148–1158. [PubMed: 23086237]

31. Bates M, Huang B, Dempsey GT, Zhuang X. Multicolor super-resolution imaging with photo-switchable fluorescent probes. Science. 2007; 317:1749–1753. [PubMed: 17702910]

32. Huang B, Wang W, Bates M, Zhuang X. Three-dimensional super-resolution imaging by stochastic optical reconstruction microscopy. Science. 2008; 319:810–813. [PubMed: 18174397]

33. Alcedo J, Ayzenzon M, Von Ohlen T, Noll M, Hooper JE. The Drosophila smoothened gene encodes a seven-pass membrane protein, a putative receptor for the hedgehog signal. Cell. 1996; 86:221–232. [PubMed: 8706127]

34. Rohatgi R, Milenkovic L, Scott MP. Patched1 regulates hedgehog signaling at the primary cilium. Science. 2007; 317:372–376. [PubMed: 17641202]

35. Corbit KC, et al. Vertebrate Smoothened functions at the primary cilium. Nature. 2005; 437:1018–1021. [PubMed: 16136078]

36. Hahn H, et al. Mutations of the human homolog of Drosophila patched in the nevoid basal cell carcinoma syndrome. Cell. 1996; 85:841–851. [PubMed: 8681379]

37. Johnson RL, et al. Human homolog of patched, a candidate gene for the basal cell nevus syndrome. Science. 1996; 272:1668–1671. [PubMed: 8658145]

38. Goodrich LV, Milenkovic L, Higgins KM, Scott MP. Altered neural cell fates and medulloblastoma in mouse patched mutants. Science. 1997; 277:1109–1113. [PubMed: 9262482]

39. Raffel C, et al. Sporadic medulloblastomas contain PTCH mutations. Cancer Res. 1997; 57:842–845. [PubMed: 9041183]

40. Milenkovic L, et al. Single-molecule imaging of Hedgehog pathway protein Smoothened in primary cilia reveals binding events regulated by Patched1. Proc Natl Acad Sci USA. 2015; 112:8320–8325. [PubMed: 26100903]

41. Chen JK, Taipale J, Young KE, Maiti T, Beachy PA. Small molecule modulation of Smoothened activity. Proc Natl Acad Sci USA. 2002; 99:14071–14076. [PubMed: 12391318]

42. Ou Y, et al. Adenylate cyclase regulates elongation of mammalian primary cilia. Exp Cell Res. 2009; 315:2802–2817. [PubMed: 19576885]

43. Bishop GA, Berbari NF, Lewis J, Mykytyn K. Type III adenylyl cyclase localizes to primary cilia throughout the adult mouse brain. J Comp Neurol. 2007; 505:562–571. [PubMed: 17924533]

44. Wong ST, et al. Disruption of the type III adenylyl cyclase gene leads to peripheral and behavioral anosmia in transgenic mice. Neuron. 2000; 27:487–497. [PubMed: 11055432]

45. Livera G, et al. Inactivation of the mouse adenylyl cyclase 3 gene disrupts male fertility and spermatozoon function. Mol Endocrinol. 2005; 19:1277–1290. [PubMed: 15705663]

46. Wang Z, et al. Adult type 3 adenylyl cyclase-deficient mice are obese. PLoS ONE. 2009; 4:e6979. [PubMed: 19750222]

47. Deane JA, Cole DG, Seeley ES, Diener DR, Rosenbaum JL. Localization of intraflagellar transport protein IFT52 identifies basal body transitional fibers as the docking site for IFT particles. Curr Biol. 2001; 11:1586–1590. [PubMed: 11676918]

48. Stratigopoulos G, et al. Hypomorphism for RPGRIP1L, a ciliary gene vicinal to the FTO locus, causes increased adiposity in mice. Cell Metab. 2014; 19:767–779. [PubMed: 24807221]

49. Parisi MA, et al. The NPHP1 gene deletion associated with juvenile nephronophthisis is present in a subset of individuals with Joubert syndrome. Am J Hum Genet. 2004; 75:82–91. [PubMed: 15138899]

50. Cantagrel V, et al. Mutations in the cilia gene ARL13B lead to the classical form of Joubert syndrome. Am J Hum Genet. 2008; 83:170–179. [PubMed: 18674751]

51. Dixon-Salazar T, et al. Mutations in the AHI1 gene, encoding jouberin, cause Joubert syndrome with cortical polymicrogyria. Am J Hum Genet. 2004; 75:979–987. [PubMed: 15467982]

52. Ferland RJ, et al. Abnormal cerebellar development and axonal decussation due to mutations in AHI1 in Joubert syndrome. Nat Genet. 2004; 36:1008–1013. [PubMed: 15322546]

53. Vierkotten J, Dildrop R, Peters T, Wang B, Rüther U. Ftm is a novel basal body protein of cilia involved in Shh signalling. Development. 2007; 134:2569–2577. [PubMed: 17553904]

54. Dani A, Huang B, Bergan J, Dulac C, Zhuang X. Superresolution imaging of chemical synapses in the brain. Neuron. 2010; 68:843–856. [PubMed: 21144999]

55. Kanchanawong P, et al. Nanoscale architecture of integrin-based cell adhesions. Nature. 2010; 468:580–584. [PubMed: 21107430]

56. Szymborska A, et al. Nuclear pore scaffold structure analyzed by super-resolution microscopy and particle averaging. Science. 2013; 341:655–658. [PubMed: 23845946]

57. Yee LE, et al. Conserved Genetic Interactions between Ciliopathy Complexes Cooperatively Support Ciliogenesis and Ciliary Signaling. PLoS Genet. 2015; 11:e1005627. [PubMed: 26540106]

58. Goetz SC, Anderson KV. The primary cilium: a signalling centre during vertebrate development. Nat Rev Genet. 2010; 11:331–344. [PubMed: 20395968]

59. Dafinger C, et al. Mutations in KIF7 link Joubert syndrome with Sonic Hedgehog signaling and microtubule dynamics. J Clin Invest. 2011; 121:2662–2667. [PubMed: 21633164]

60. Hynes AM, et al. Murine Joubert syndrome reveals Hedgehog signaling defects as a potential therapeutic target for nephronophthisis. Proc Natl Acad Sci USA. 2014; 111:9893–9898. [PubMed: 24946806]

61. You Y, Brody SL. Culture and differentiation of mouse tracheal epithelial cells. Methods Mol Biol. 2013; 945:123–143. [PubMed: 23097105]

62. Bossi M, et al. Multicolor far-field fluorescence nanoscopy through isolated detection of distinct molecular species. Nano Lett. 2008; 8:2463–2468. [PubMed: 18642961]

63. TAUBIN G. Estimation of Planar Curves, Surfaces, and Nonplanar Space-Curves Defined by Implicit Equations with Applications to Edge and Range Image Segmentation. Ieee Transactions on Pattern Analysis and Machine Intelligence. 1991; 13:1115–1138.

64. Fienup JR, Guizar-Sicairos M, Thurman ST. Efficient subpixel image registration algorithms. Opt Lett OL. 2008; 33:156–158.

65. Schneider CA, Rasband WS, Eliceiri KW. NIH Image to ImageJ: 25 years of image analysis. Nat Methods. 2012; 9:671–675. [PubMed: 22930834]

66. Pieper U, et al. ModBase, a database of annotated comparative protein structure models and associated resources. Nucleic Acids Res. 2014; 42:D336–46. [PubMed: 24271400]

67. Webb B, Sali A. Comparative Protein Structure Modeling Using MODELLER. Curr Protoc Bioinformatics. 2016; 54:5.6.1–5.6.37. [PubMed: 27322406]

68. Tsirigos KD, Peters C, Shu N, Käll L, Elofsson A. The TOPCONS web server for consensus prediction of membrane protein topology and signal peptides. Nucleic Acids Res. 2015; 43:W401–7. [PubMed: 25969446]

69. Drozdetskiy A, Cole C, Procter J, Barton GJ. JPred4: a protein secondary structure prediction server. Nucleic Acids Res. 2015; 43:W389–94. [PubMed: 25883141]
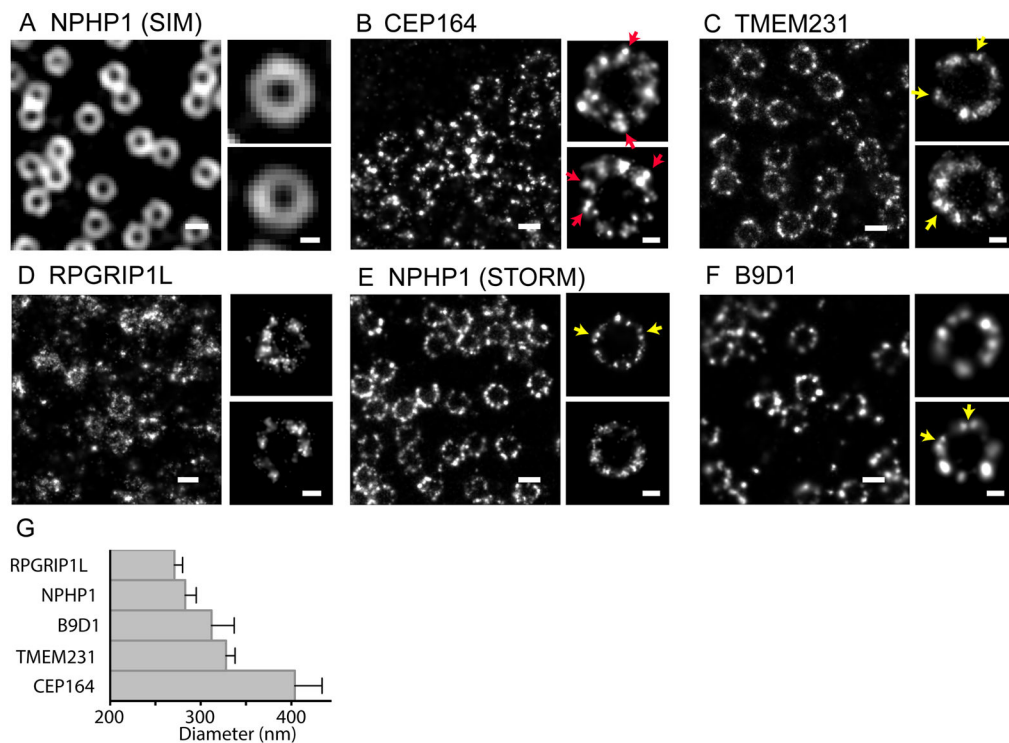
Figure 1. MKS and NPHP complexes form rings of discrete puncta
(**A**) SIM detection of NPHP1 in mTECs reveals a ring structure. STORM detection of (**B**) CEP164, (**C**) TMEM231, (**D**) RPGRIP1L, (**E**) NPHP1, and (**F**) B9D1 in mTECs reveals that the rings are comprised of discrete puncta. MKS complex components and NPHP1 are present in doublets oriented tangentially to the ring circumference (yellow arrows). In contrast, STORM imaging of CEP164, a distal appendage component, reveals clusters oriented obliquely to the ring circumference (red arrows). (**G**) Diameter measurements of rings in STORM images. CEP164: 404 ± 30nm, n = 31 ring structures. TMEM231: 328 ± 10nm, n = 30 ring structures. B9D1: 312 ± 25nm, n = 27 ring structures. NPHP1: 283 ± 12nm, n = 46 ring structures. RPGRIP1L: 271 ±9 nm, n = 23 ring structures. Data are the mean ± standard deviation. P < 0.0001 for any pair of values. Scale bars are 300nm and 100nm for multiple-structure images and single structure images, respectively.
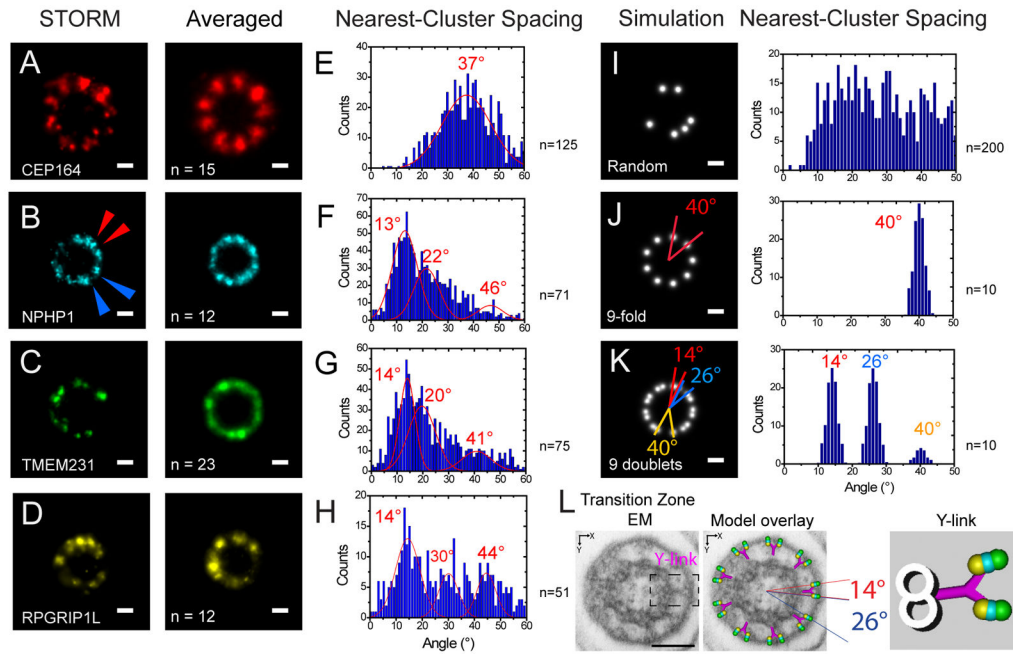
Figure 2. MKS and NPHP complex rings are comprised of doublets

A–D: STORM images of mTEC cilia stained for (**A**) CEP164, (**B**) NPHP1, (**C**) TMEM231, or (**D**) RPGRIP1L (left). Multiple images of individual ring structures were aligned by cross correlation and averaged (right). The number of STORM images used for averaging are CEP164: 15, NPHP1: 12, TMEM231; 23 and RPGRIP1L; 12.. **E-H:** Histograms of the angular spacing between the nearest clusters of (**E**) CEP164, (**F**) NPHP1, (**G**) TMEM231, and (**H**) RPGRIP1L rings. Peak positions at $37 \pm 2°$ (n = 125) for CEP164, $13 \pm 1°$ and $23 \pm 2°$ for NPHP1 (n = 71), $14 \pm 1°$ and $20 \pm 1°$ for TMEM231 (n = 75), and $14 \pm 1°$ and $30 \pm 1°$ for RPGRIP1L (n = 51). n represents number of STORM images used for the analysis. Uncertainty calculated by bootstrapping, data are mean ± standard error of the mean. **I-K:** Histograms of the angular spacing of between the nearest clusters of simulated rings in which the puncta are (**I**) randomly distributed along the ring circumference, (**J**) nine-fold symmetric, and (**K**) comprised of nine-fold symmetric doublets. n represents number of simulated rings used for the analysis. (**L, left**) Transmission electron micrograph (TEM) of a transverse section through the transition zone of a mouse ependymal cell cilium. A Y-link is highlighted by a dashed line. The mean and standard deviation of the angle between the tips of Y-links was $20 \pm 2.3°$, n = 70 Y-links analyzed. (**L, center**) Overlay of a model of angular and radial arrangement of transition zone proteins with the TEM. (**L, right**) A model of the radial and angular distributions of transition zone proteins superimposed onto a Y-link structure. Scale bars, 100nm.
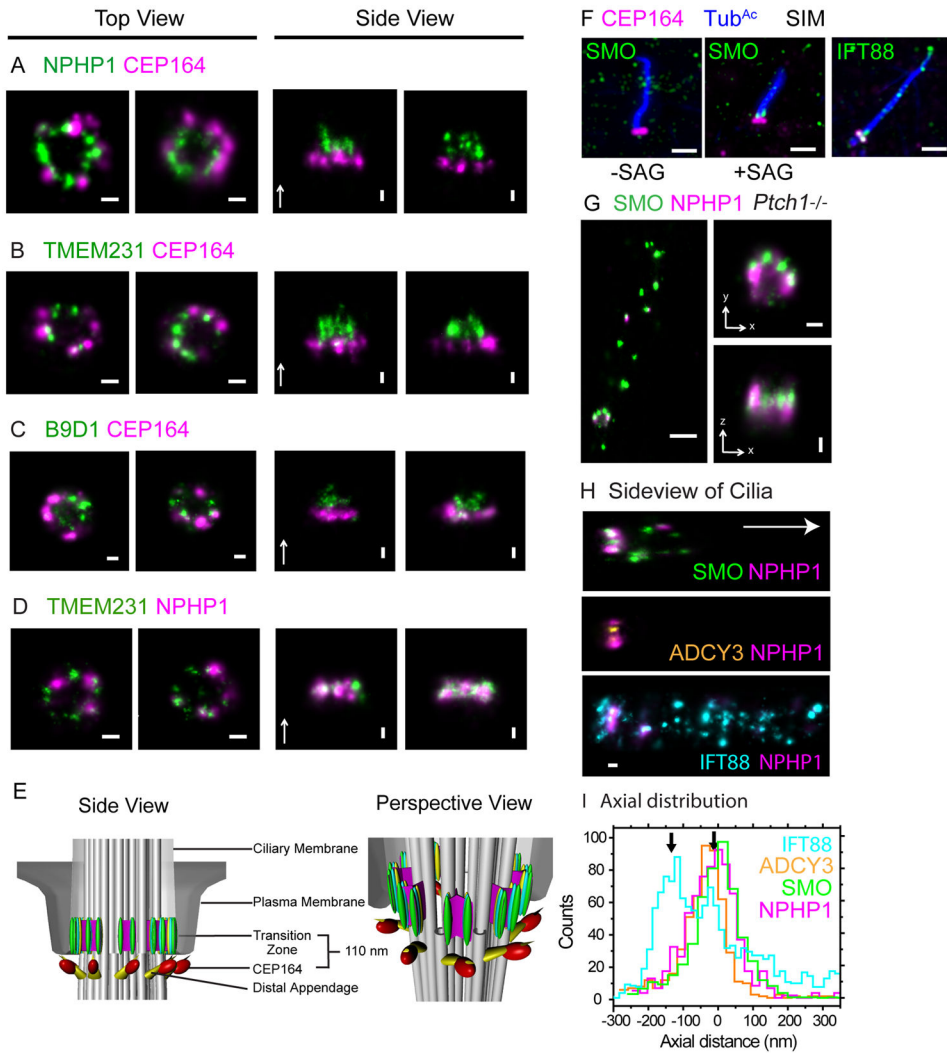
Figure 3. MKS and NPHP complexes occupy the same proximodistal position in the transition zone, where SMO docks upon Hedgehog pathway activation

(**A–C**) Two-color STORM images of CEP164 (magenta) and (**A**) NPHP1 (green), (**B**) TMEM231 (green), and (**C**) B9D1 (green). Top views (left) are of mTECs (top views) and side views are of IMCD3 cells. The arrows in the side views point in the direction of the ciliary tip. Scale bars, 100nm. The NPHP1 ring thickness is 122 ± 36nm (width at half maximum of the Gaussian fitting; mean±standard deviations for distance and thickness measurements) and is 103 ± 36nm distal to the CEP164 ring (n=5). TMEM231 ring thickness = 114 ± 61 (n=12). B9D1 ring thickness = 97 ±5 0nm (n=5). TMEM231 and B9D1 rings are 115 ± 16nm (n=12) and 91 ± 40nm (n=5) distal to CEP164, respectively. n represents number of STORM images used for the analysis (**D**) Two-color STORM images of TMEM231 (green) and NPHP1 (magenta). Scale bars, 100nm. (**E**) Side view and perspective view of a 3D model of the ciliary gate including the microtubules of the basal body and axoneme (gray), CEP164 along the distal appendages (yellow), and TMEM231 (green), NPHP1 (teal) and RPGRIP1L (yellow) within the transition zone. (**F, left & middle**) SIM image of human fibroblasts stained for SMO (green), CEP164 (magenta) and

acetylated tubulin (blue) treated with or without SAG. Scale bar, 1 μm. (**F, right**) SIM image of human fibroblasts stained for IFT88 (green), CEP164 (magenta) and acetylated tubulin (blue). Scale bar, 1 μm. (**G**) Two-color STORM of SMO (green) and NPHP1 (magenta) in *Ptch1*$^{-/-}$ MEFs. Scale bars, 500nm (left), 100nm (right). (**H**) Two-color STORM of side views of primary cilia. SMO (green) and NPHP1 (magenta) were imaged in *Ptch1*$^{-/-}$ MEFs. ADCY3 (orange) and NPHP1 (magenta) and were imaged in WT MEFs. The arrow points in the direction of the ciliary tip. Scale bar, 100nm. (**I**) Histogram of the intensity of SMO (green), ADCY3 (orange), NPHP1 (magenta), and IFT88 (cyan) along the axonemal direction, corresponding to images of which (**H**) is representative.
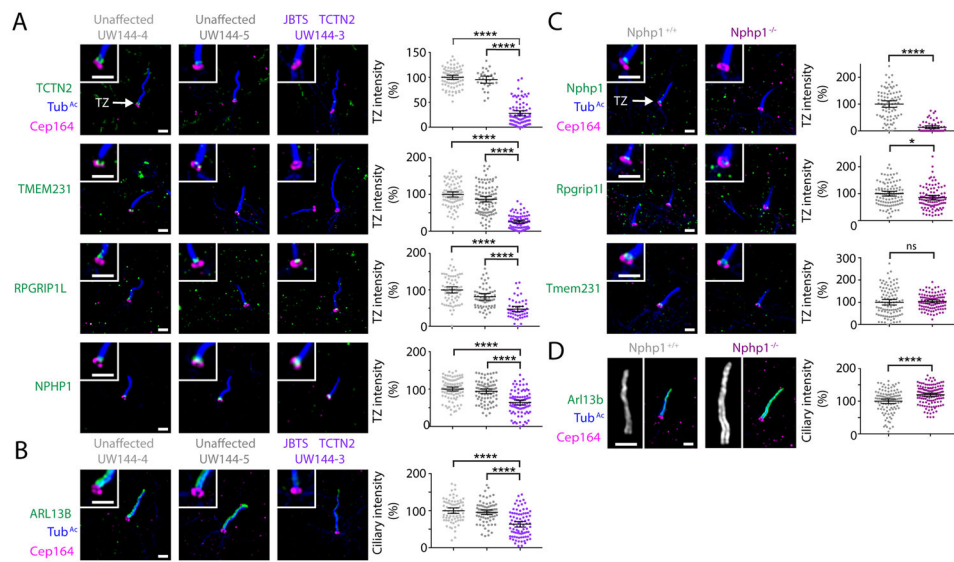
Figure 4. MKS and NPHP complexes are displaced from the transition zone in a Joubert syndrome patient with mutations in *TCTN2*

(**A**) SIM images of acetylated tubulin (Tub^{Ac}, blue), CEP164 (magenta) and TCTN2, TMEM231, RPGRIP1L, or NPHP1 (green) in fibroblasts from a JBTS-affected individual and two unaffected siblings. Quantification of TCTN2, TMEM231, RPGRIP1L, and NPHP1 fluorescence intensity at the transition zone (right). Data pooled from two independent experiments. n = number of transition zones measured (individuals 144-4, 144-5, 144-3): TCTN2 (82, 29, 82), TMEM231 (90, 105, 86), RPGRIP1L (74, 62, 50), and NPHP1 (100, 82, 87). The differences (144-4 vs 144-3) are 72 ± 3% for TCTN2, 75 ± 5% for TMEM231, 36 ± 4% for NPHP1, and 53 ± 6% for RPGRIP1L. (**B**) SIM images of acetylated tubulin (blue), CEP164 (magenta) and ARL13B (green). Quantification of ciliary ARL13B fluorescence intensity (right). Data pooled from two independent experiments. n = number of cilia measured (144-4, 144-5, 144-3: 72, 78, 84). The difference (144-4 vs 144-3) is 37 ± 5%. (**C**) SIM images of Tub^{Ac} (blue), CEP164 (magenta) and NPHP1, RPGRIP1L, and TMEM231 (green) in *Nphp1$^{+/+}$* and *Nphp1$^{-/-}$* mouse embryonic fibroblasts. Quantification of Nphp1, Rpgrip1l, and Tmem231 fluorescence intensity at the transition zone (right). Data pooled from three independent experiments. n = number of transition zones measured (*Nphp1$^{+/+}$*, *Nphp1$^{-/-}$*): NPHP1 (83, 59), RPGRIP1L (102, 102), and TMEM231 (100, 98). The difference (*Nphp1$^{+/+}$* vs *Nphp1$^{-/-}$*) is 100 ± 8% for NPHP1, 15 ± 6% for RPGRIP1L, and 4 ± 7% for TMEM231. (**D**) SIM images of Tub^{Ac} (blue), CEP164 (magenta) and ARL13B (green). Quantification of ciliary Arl13b fluorescence intensity (right). Mean±95% confidence interval are pooled data from three independent experiments. n = number of cilia measured (*Nphp1$^{+/+}$*, *Nphp1$^{-/-}$*; 105, 133). The difference (*Nphp1$^{+/+}$* vs *Nphp1$^{-/-}$*) is −20 ± 4%. ns, not significant. *, P value = 0.021. ****, P value <0.0001. Multiple comparisons were ordinary one-way ANOVAs with Tukey's test for pairwise differences. Two sample comparisons by two-tailed unpaired t-test. Mean ± standard error reported for all graphs. Scale bars, 1 μm. Statistics source data for all panels are available in Supplementary Table S2.
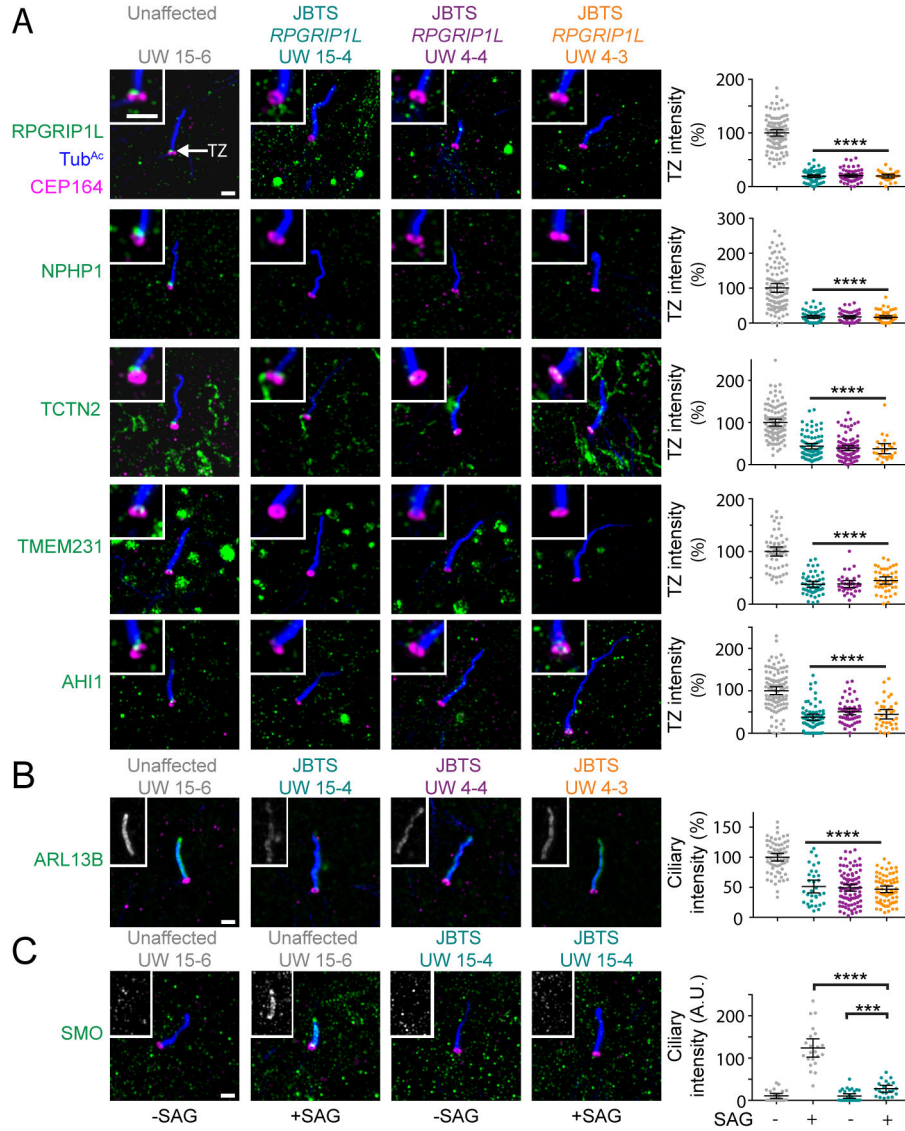
Figure 5. MKS and NPHP complexes are displaced from the transition zone in Joubert syndrome patients with mutations in *RPGRIP1L*

(**A**) SIM images of acetylated tubulin (Tub^{Ac}, blue), CEP164 (magenta) and RPGRIP1L, NPHP1, TCTN2, TMEM231 or AHI1 (green) in fibroblasts from three JBTS-affected individuals and an unaffected sibling. Quantification of RPGRIP1L, NPHP1, TCTN2, TMEM231 and AHI1 fluorescence intensity at the transition zone (right). Mean±95% confidence interval are pooled data from three independent experiments. n = number of transition zones measured (individuals 15-6, 15-4, 4-4, 4-3): RPGRIP1L (100, 65, 62, 28), NPHP1 (101, 58, 53, 53), TCTN2 (102, 80, 92, 24), TMEM231 (58, 50, 33, 43), and AHI1 (100, 69, 55, 36). Mean difference (15-6 vs 15-4) is 81 ± 3% for RPGRIP1L, 85 ± 7% for NPHP1, 36 ± 4% for NPHP1, and 56 ± 5% for TCTN2, 62 ± 5% for TMEM231, and 65 ± 6% for AHI1. (**B**) SIM images of Tub^{Ac} (blue), CEP164 (magenta) and ARL13B (green). Quantification of ciliary ARL13B fluorescence intensity (right). Mean ± 95% confidence interval are pooled data from three independent experiments. n = number of cilia measured

(15-6, 15-4, 4-4, 4-3; 67, 33, 94, 68). Mean difference (15-6 vs 15-4) is 49 ± 6%. (**C**) SIM images of Tub^{Ac} (blue), CEP164 (magenta) and SMO (green) in fibroblasts from a JBTS-affected individual and an unaffected sibling in the presence or absence of SAG. Quantification of ciliary SMO fluorescence intensity (right). Mean ± 95% confidence interval is shown in graph. Two independent experiments were performed and data were pooled. n = number of cilia measured (15-6 no SAG, 15-6 +SAG, 15-4 no SAG, 15-4 +SAG; 23, 22, 29, 21). Mean difference (15-6 +SAG vs 15-4 +SAG) is 78 ± 9%. ***, P value = 0.0003. ****, P value < 0.0001. Multiple comparisons were ordinary one-way ANOVAs with Tukey's test for pairwise differences. Two sample comparisons were performed using a two-tailed unpaired t test. Mean difference ± standard error of difference reported for difference analysis. n values used in difference analysis same as for measurements. Scale bars, 1 μm. Statistics source data for all panels are available in Supplementary Table S2.
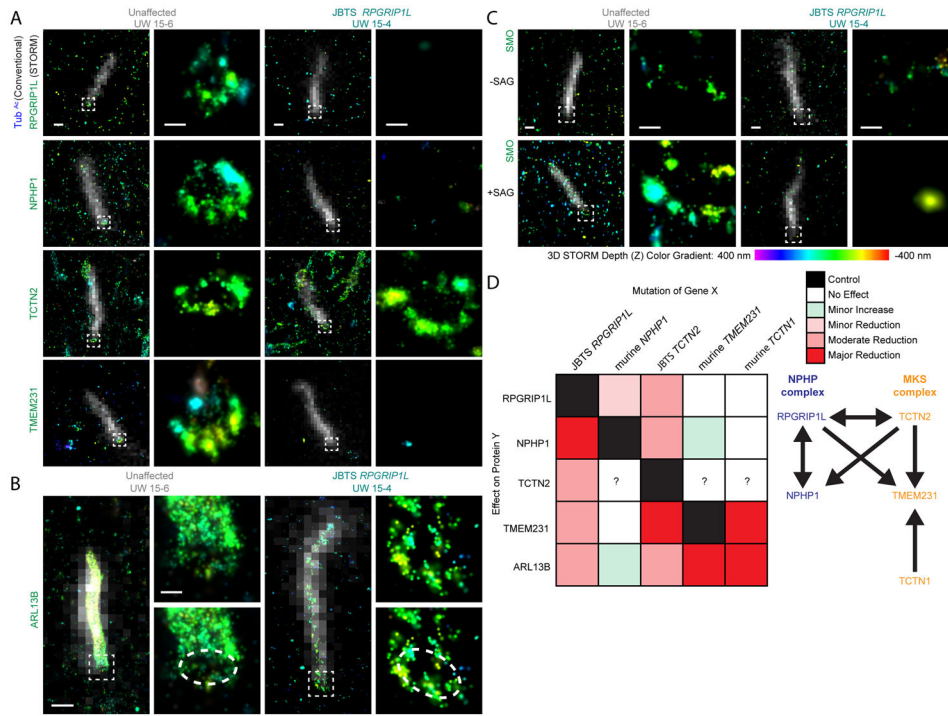
Figure 6. Transition zone rings formed by MKS and NPHP complexes are disrupted in a Joubert syndrome patient with mutations in *RPGRIP1L*

(**A**) Conventional epifluorescence images of acetylated tubulin (Tub^Ac, white) overlaid on STORM images of RPGRIP1L, NPHP1, TCTN2, and TMEM231 (colored according to 3D STORM depth color gradient) in fibroblasts from a JBTS-affected individual with mutations in *RPGRIP1L* and an unaffected sibling. White boxes indicate location of the transition zone, magnified and displayed alongside the overlayed images. (**B**) Conventional epifluorescence images of acetylated tubulin (white) overlaid on STORM images of ARL13B (3D color gradient). Ring at the ciliary base is magnified and displayed alongside the overlayed images. Dashed line indicates ring pattern. (**C**) Conventional epifluorescence images of Tub^Ac (white) overlaid on STORM images of SMO in fibroblasts from a JBTS-affected individual and an unaffected sibling in the presence or absence of SAG. White boxes indicate location of the transition zone, magnified and displayed alongside the overlayed images. (**D**) Chart and model depicting the structural interdependence between the NPHP and MKS complexes. Left, mutation of *RPGRIP1L*, *NPHP1*, *TCTN2*, *TMEM231*[16,20], or *TCTN1*[14] has a specified effect on the levels of protein Y in the transition zone (RPGRIP1L, NPHP1, TCTN2, and TMEM231) or the cilium (ARL13B). ?, undetermined effect. Right, arrows indicating dependencies in transition zone protein localization. Scale bars, 500nm for images overlayed with acetylated tubulin, and 100nm for magnified images.